# Temperature correction of radiometric and geometric models for an uncooled CCD camera in the Near Infrared

Thierry Sentenac[†], Yannick Le Maoult[†], Guy Rolland[‡] and Michel Devy[⋆]

**Abstract**

This paper presents radiometric and geometric models for both temperature and displacement non-contact measurements using an uncooled Charge-Coupled Device (CCD) video camera. Such techniques "one sensor-two measures" represent an interest in many industrial low-cost applications and scientific domains.
To benefit from both measurements, we have to use the camera's spectral response in the near infrared spectral band ($NIR$) from 0.75 micrometer to 1.1 micrometer. In this spectral band, the temperature variations of an uncooled CCD camera are taken into account in the radiometric and geometric models. By using physical models for CCD camera, we quantify detector's quantum efficiency, sensor noise and spatial resolution as a function of the wavelength and of the detector temperature. These models are confirmed by experimental results of calibration with a low-cost uncooled camera based on a Sony detector and operating over the detector temperature range of $-30°C$ to $+50°C$.

**Keywords**

CCD cameras, camera calibration, sensor modeling, temperature, noise estimation, radiometric model, geometric model, spatial resolution, Modulation Transfer Function ($MTF$).

## I. Introduction

OVER recent years, the material research center of the Ecole des Mines d'Albi-Carmaux (CROMeP) has developed temperature gradient measurements based on infrared thermographic cameras [1]. In the same time, a team has been involved in $3D$ deformation [2] and distortion [3] measurements using CCD cameras. To improve maintenance and cost in industrial applications, we have to measure both temperature and dimensional characteristics using only one non-contact sensor. The system must be able to measure a temperature from $350°C$ to $1000°C$ with a tolerance of $\pm 25°C$ and spatial surface deformations of $\pm 0.1\,mm$ with an observation distance of $1\,m$.
However, the main difficulty is the temperature measurement. Adopted from the spectral photon luminance $L_s$ of a real source [4], the sensor operates in the infrared spectral band. The luminance is described by the Planck's radiation law as follows:

[†]Ecole des Mines d'Albi-Carmaux, 81 013 ALBI CT Cedex 09, FRANCE, E-mail: sentenac@enstimac.fr
[‡]Centre National d'Etudes Spatiales, 31 401 TOULOUSE Cedex 04, FRANCE, E-mail: guy.rolland@cnes.fr.
[⋆]Laboratoire d'Analyse et d'Architecture des Systèmes, 31 077 TOULOUSE Cedex 04, FRANCE, E-mail: michel@laas.fr.

$$L_s(\lambda,T) = \varepsilon \frac{C_3 \lambda^{-4}}{\exp\left(\frac{C_2}{\lambda T}\right) - 1} \quad (1)$$

where $T$ is the absolute temperature ($Kelvin$), $\varepsilon$ is the emissivity of the source, $h$ is Planck's constant ($h = 6.62\,10^{-34}\,J\,s$), $c$ is the speed of light ($c = 3\,10^{8}\,m/s$) and $k$ is Boltzmann's constant ($k = 1.3807\,10^{-23}\,J/K$). Finally, the second and the third radiation constants are respectively given by $C_2 = \frac{h\,c}{k}\,\mu m\,K$ and $C_3 = 2\,c$. Thus, applying relation (1) when temperature $T$ equals $350°C$ (and respectively $1000°C$), the luminance reaches a peak at a wavelength value of $4.65\,\mu m$ (and respectively $2.25\,\mu m$). But, the traditional $3 - 5\mu m$ infrared cameras, are often limited by their fragility, high cost and low spatial resolution. In the Near Infrared spectral band ($NIR$) ($0.75 - 1.1\mu m$), luminance values (from $10^{16}$ to $2 \times 10^{21}\,photons/s\,m^2\,sr\,\mu m$) allow a measurement of a temperature from $350°C$ to $1000°C$. Moreover, Charge-Coupled Device cameras (CCD) operating in $NIR$ spectral band are relatively low cost, light weight, compact and have high spatial resolution. They can measure through a glass window and present less sensitivity to uncertainties concerning the emissivity of the object. A few industrial applications with low-cost CCD cameras related to high-temperature measurement over the range $[800 - 1800°C]$ are reported in [5] and [6]. In this paper, our objective is to measure temperatures below the usual value of $800°C$, in low illuminated conditions with noise considerations like in [7]. Additionally, the new radiometric model presented in this paper takes into account the variation of the detector temperature of low-cost uncooled CCD devices widely used in industrial situations. This radiometric model is based on the study of CCD sensor properties like quantum efficiency and noise.

Moreover, we examine the spatial resolution changes in $NIR$ spectral band for the same range of temperatures. From the study of the Modulation Transfer Function ($MTF$), we deduce the influence of wavelength and detector temperature on the intrinsic parameters required in the "pin-hole" geometric model [8] used in our applications. Finally, after characterization and calibration procedures, some advantages and limitations of this strategy of "one sensor-two measurements" are discussed.

## II. Radiometric model

The radiometric model is determined by a formal relationship between the temperature $T$ of an ideal blackbody source and the analog $V_c$ or digital $I_D$ camera CCD output. Usually, the model is used with infrared cameras and can be directly applied with cooled CCD cameras. However, uncooled cameras are characterized by a temperature detector variation $T_d$ which involves sensor noise and quantum efficiency $\eta_e$ modifications mainly due to the variation of the absorption light. As a result, the model parameters depend on detector temperature, and a temperature calibration allows determining their values. In this section, we present results in the case of a camera based on a Sony detector.

### A. Temperature-signal relation

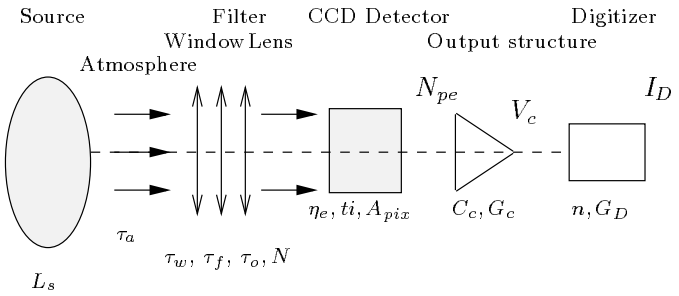


Fig. 1. Temperature calibration situation (parameters are explained in text).

Figure 1 illustrates an imaging CCD directly viewing a hot source with a photon luminance $L_s$ during integration time $ti$. Ideally, such a system produces a number of photoelectrons $N_{pe}$ at a collection site given

by:

$$N_{pe} = K_o\, ti \int_{\Delta\lambda} \tau_a(\lambda)\tau_w(\lambda)\tau_f(\lambda)\tau_o(\lambda)L_s(\lambda)\eta_e(\lambda, T_d)d\lambda \tag{2}$$

where $K_o$ is the optical focused magnification ($K_o = \frac{\pi\, A_{pix}}{4\, N^2}$), $N$ is the F-number, and $A_{pix}$ is the sensitive pixel area. $\tau_a$, $\tau_w$, $\tau_f$, $\tau_o$ are respectively atmospheric, window glass, near infrared filter and optical system transmittance. $\eta_e$ is the detector's quantum efficiency ($e^-/photons$). Such a model can be improved: for example, [9] describes nonlinearities in short exposure time ($<\ 40\, ms$) due to the mechanical nature of the shutter mechanism.

The charge packets integrated at each collection site are transferred in parallel with a charge transfer efficiency ($CTE \approx 1$) into an output register. Before the next parallel transfer, the register transfers each of its charge packets to a floating diode acting as a capacitor $C_c$. The difference voltage $V_c$ of the capacitor is amplified with a gain $G_c$, and the final value is linearly proportional to the number of electrons $N_{pe}$.

$$V_c = \frac{G_c}{C_c}\, q\, N_{pe}(\lambda, T_d) \tag{3}$$

where $q$ is the electronic charge ($q = 1.6\, 10^{-19}\ Coulomb$).

Finally, the signal generated by the camera CCD (full range value is named $V_{cFR}$) is converted into a digital signal $I_D$ with a resolution of $n$ bits and is amplified with a gain $G_D$.

$$I_D = \frac{G_D\, 2^n}{V_{cFR}}\, V_c(\lambda, T_d) \tag{4}$$

Relation (4) shows that the output signal $I_D$ depends on the spectral quantum efficiency and on transmission and source characteristics. From this relation, the radiometric model can be determined using the following steps:

1. In case of a CCD detector operating in $NIR$ spectral band, a very small wavelength range $\Delta\lambda$ equal to $0.35\mu m$ is selected. The integral can then be computed around an effective wavelength $\lambda_e$. $L_s$ will only vary in the source temperature $T$ ($L_s(\lambda_e, T)$), and $\eta_e$ depends only on the detector temperature ($\eta_e(\lambda_e, T_d)$).
2. During the temperature calibration procedure with a controlled atmosphere and with the same window, filter and optical system, we can consider transmittances $\tau_a, \tau_w, \tau_f$ and $\tau_o$ as constants. On our system, only F-number $N$, exposure time $ti$ and Analog-to-Digital converter gain $G_D$ can be modified.

$$I_D = A_1\, \frac{G_D\, ti}{N^2}\, L_s(\lambda_e, T)\, \eta_e(\lambda_e, T_d) \tag{5}$$

where $A_1$ is a constant ($A_1 = \tau_a\tau_w\tau_f\, \tau_o\, \frac{2^n}{V_{cFR}}\, \frac{G_c}{C_c}\, q\, \frac{\pi\, A_{pix}}{4}$)

3. The luminance $L_s(\lambda_e, T)$ is described by the Planck's blackbody radiation law (1) with an emissivity $\varepsilon_{BB} \approx 1$.

$$I_D = \frac{A_2\, \frac{G_D\, ti}{N^2}}{\exp\left(\frac{B}{T}\right) - 1}\, \eta_e(\lambda_e, T_d) \tag{6}$$

where $A_2$ and $B$ are constants ($A_2 = A_1\, \varepsilon_{BB}\, C_3\, \lambda_e^{-4}$ and $B = \frac{C_2}{\lambda_e}$).

4. Moreover, we introduce in relation (6) a variable $D$ to model the continuous value of camera output in a dark environment. The value of $D$ also depends on the effect of noise sources of the CCD imaging system which are highly linked to the detector temperature.

Finally, the temperature-signal relation is described by:

$$I_D = \frac{A_2\, \frac{G_D\, ti}{N^2}\, \eta_e(\lambda_e, T_d)}{\exp\left(\frac{B}{T}\right) - 1} + D(T_d) \tag{7}$$

### B. Detector's quantum efficiency model $\eta_e$

The detector's quantum efficiency is defined as the ratio of electron flux $N_{pe}$ to incident photon flux $N_p$ onto the optical system for a single collection site and a particular exposure time:

$$\eta_e(\lambda_e, T_d) = \frac{N_{pe}(\lambda_e, T_d)}{N_p} \tag{8}$$

In photomos devices, we can approximate the quantum efficiency by that of an abrupt half junction. We

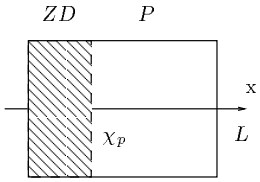


Fig. 2. Cross section of photomos structure.

assume that the front part of the photomos structure is close to zero (see Figure 2). The quantum efficiency is then defined by the sum of the depletion region $ZD$ efficiency ($\eta_{ZD}$) and back region $P$ efficiency ($\eta_P$). With reference to [10], $\eta_{ZD}$ and $\eta_P$ are given by:

$$\eta_{ZD} = 1 - \exp(-\alpha\,\chi_p) \tag{9}$$

$$\eta_P = \frac{(\alpha\,L_n)^2}{(\alpha\,L_n)^2-1}\left(\exp(-\alpha\,\chi_p) + \frac{\exp(-\alpha\,L)-\exp(-\alpha\,\chi_p)\,\cosh(\frac{L-\chi_p}{L_n})}{\alpha\,L_n\sinh(\frac{L-\chi_p}{L_n})}\right) \tag{10}$$

where $L_n$, $L$, $\chi_p$ are respectively electron diffusion length in region $P$ ($mm$), substrate length ($mm$) and limit of depletion region ($mm$). $\alpha$ represents the absorption photon coefficient in the silicon part (see formula in Appendix). Figure 3 shows the evolution of this coefficient versus the wavelength at different temperatures. It decreases with an increasing wavelength and a decreasing temperature.
Therefore, the quantum efficiency of the detector is defined as a function of the wavelength and the temperature owing to absorption coefficient characteristics.

$$\eta_e = 1 + \exp(-\alpha\,L)\left(\frac{K_a}{K_b}\right) + \exp(-\alpha\,\chi_p)\left(\frac{K_a}{K_b}\left(K_b - \frac{K_b}{K_a} - \cosh(\frac{L-\chi_p}{L_n})\right)\right) \tag{11}$$

where $K_a$ and $K_b$ are variable $\left(K_a = \frac{(\alpha\,L_n)^2}{(\alpha\,L_n)^2-1}\right.$ and $\left.K_b = \alpha\,L_n\sinh(\frac{L-\chi_p}{L_n})\right)$.
To model the quantum efficiency of the detector, we have to determine the internal parameters ($L_n$, $L$ and $\chi_p$) of the detector. However, these parameters can generally not be accessed easily. One solution can be to measure the quantum efficiency and to fit the parameters of model (11). Another way to deal with this problem is to correct the constant value of the quantum efficiency known at a reference temperature $T_{dref}$ with a law $f(\lambda, T_d)$ versus the wavelength and the temperature, as shown in (12).

$$\eta_e(\lambda, T_d) = \eta_e(\lambda, T_{dref})\,f(\lambda, T_d) \tag{12}$$

In $NIR$ spectral band, the expression of $f$ is obtained from relation (11) and is defined by a macroscopic diffusion law as follows:

$$f = f_2(T_d)\left(\exp\left(f_1(\lambda, T_d)\right) + \exp\left(-f_1(\lambda, T_d)\right)\right)^{sign} \tag{13}$$

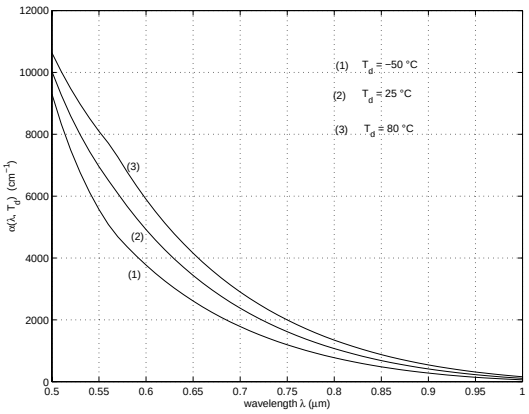


Fig. 3. $\alpha$ as a function of $\lambda$ and $T_d$.

where $sign$ is equal to 1 when $(T_d - T_{dref}) \geq 0$ and $-1$ on the contrary, while $f_1$ is given by:

$$f_1(\lambda, T_d) = K_1 \left(\lambda_{norm}\right)^{K_2} \left(T_{dnorm}\right)^{K_3} \tag{14}$$

where:
• $\lambda_{norm} = \frac{\lambda - \lambda_{min}}{\lambda_{max}(T_d) - \lambda_{min}}$, $\lambda_{max}$ and $\lambda_{min}$ are respectively maximum and minimum wavelengths of $NIR$ spectral band ($\lambda_{max} = \frac{h\,c}{E_g(T_d)\,q}, \lambda_{min} = 0.75\,\mu m$). $E_g$ is the energy gap $(eV)$ $\left(E_g = 1.1557 - \left(\frac{7.02\,10^{-4}\,T_d^2}{1108 + T_d}\right)\right)$ (see formula in [11]).
• $T_{dnorm} = \frac{|T_d - T_{dref}|}{T_{dmax} - T_{dref}}$, $T_{dmax}$ is the maximal detector temperature.
Finally, $f_2$ is a constant $K_4$ raised to the power of normalized detector temperature $T_{dnorm}$. To obtain a ratio of 1 when $T_d = T_{dref}$, we divide this term by 2. We get:

$$f_2(T_d) = \frac{(K_4)^{T_{dnorm}}}{2} \tag{15}$$

According to the first step of the determination of the radiometric model, we compute the relation (12) at an effective wavelength $\lambda_e$:

$$\eta_e(\lambda_e, T_d) = \eta_e(\lambda_e, T_{dref})\, f(\lambda_e, T_d) \tag{16}$$

From the model (16), the temperature-signal relation (7) is modified as follows:

$$I_D = \frac{A_3 \frac{G_D\, ti}{N^2} f(\lambda_e, T_d)}{\exp\left(\frac{B}{T}\right) - 1} + D(T_d) \tag{17}$$

where $A_3$ is a constant $\left(A_3 = A_2\, \eta_e(\lambda_e, T_{dref})\right)$.

### C. Coefficient D model: Temporal source noise

We model coefficient $D$ by the sum of a constant $I_{D0}$ and a variable $\overline{I_D}$ scaling the temperature $T_d$. $I_{D0}$ is associated with an offset and with noise sources independent of temperature. We assume that noise is independent of signal level and spatial variations. Therefore, we get:

$$D(T_d) = I_{D0} + \overline{I_D}(T_d) \tag{18}$$

Many books and articles, for example [12], describe noise sources depending on the detector temperature. We have represented the main ones on Figure 4.

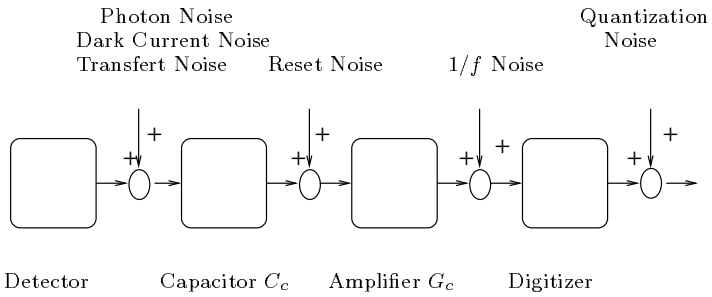


Fig. 4. Noise transfer diagram.

The main source noise comes from the dark current generated by thermal generation in silicon. It has been shown that the mean background dark current level increases with the temperature $T_d$ $(Kelvin)$ and the integration time $ti$ $(s)$ as follows:

$$V_{cdark} = ti\, A_{pix} \left( A_{dark}\, T_d^{\beta} \right)^{1/2} \exp - \frac{E_g(T_d)\, q}{2\, k\, T_d} \tag{19}$$

where $A_{dark}$ and $\beta$ are constant ($\beta = 3$ in silicon device).

Considering zero as the mean value of the reset noise, we add to the model (19) a linear dependence with temperature which comes from a drift of electronic components. Then, the mean value of the digital output $\overline{I_D}$ fluctuates with temperature as follows:

$$\overline{I_D} = G_D \left( K_5\, ti\, T_d^{3/2} \exp - \frac{E_g(T_d)\, q}{2\, k\, T_d} + K_6\, T_d \right) \tag{20}$$

where $K_5$ and $K_6$ are constant ($K_5 = \frac{2^n}{V_{cFR}}\, A_{dark}^{1/2}$).

*D. Conclusion of radiometric model expression*

Finally, equation (21) describes our complete radiometric model with 9 parameters ($A_3$, $B$, $I_{D0}$, $K_1$, $K_2$, $K_3$, $K_4$, $K_5$ and $K_6$) which must be fitted during a calibration procedure.

$$I_D = \frac{A_3 \frac{G_D\, ti}{N^2} f(\lambda_e, T_d)}{\exp\left(\frac{B}{T}\right) - 1} + D(T_d) \tag{21}$$

where:

$$\begin{aligned}
f &= f_2 \left( \exp\left(f_1\right) + \exp\left(-f_1\right) \right)^{sign} \\
f_1 &= K_1 \left(\lambda_{norm}\right)^{K_2} \left(T_{dnorm}\right)^{K_3} \\
f_2 &= \frac{(K_4)^{T_{dnorm}}}{2} \\
D &= I_{D0} + \overline{I_D}(T_d) \\
I_{D0} &= \text{constant} \\
\overline{I_D} &= G_D \left( K_5\, ti\, T_d^{3/2} \exp - \frac{E_g(T_d)\, q}{2\, k\, T_d} + K_6\, T_d \right)
\end{aligned}$$

*E. Radiometric model calibration*

First of all, from the CCD camera model (21), we estimate the dependence of the output signal noise in function of the detector temperature to fix the $I_{D0}$, $K_5$ and $K_6$ parameters. Then, to fit missing parameters, the CCD camera has been calibrated using blackbody temperatures from $320°C$ to $460°C$ intervals with detector temperature variation range $[-30, +50°C]$.

In our experiments, we have tested several kinds of CCD cameras, but we present only the results for the $VHR2000$ CCD camera manufactured by Digital Vision. The CCD is a Sony $ICX\,039\ 752(H) \times 582(V)$ array of $8.6(H) \times 8.3(V)\,\mu m^2$ pixels. This camera has a linear response with exposure time. We add a Kodak Wratten $87C$ near infrared selected filter. All experimental tests have taken place in a dark environment where the detector temperature $T_d$ was regulated with an air-conditioned enclosure.

E.1 Observations of system noise

In a dark environment and when the detector temperature $T_d$ is adjusted between $-30°C$ and $+60°C$, we compute the mean value $D$ of the digital image. Considering an exposure time $ti$ of $20\,ms$ and a unitary gain

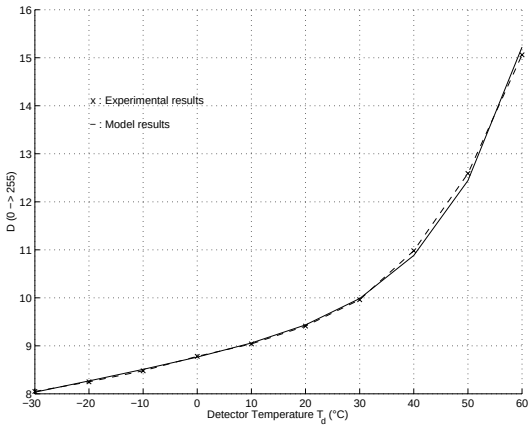


Fig. 5. $D$ as a function of $T_d$.

$G_D$, Figure 5 shows a linear evolution for $D$ until temperature reaches $20°C$. Above this temperature, $D$ increases exponentially mainly because of current noise. By fitting equation (18) to these $D$ values, we have deduced $I_{D0}$, $K_5$ and $K_6$ parameters which are provided in Table I.

This model allows estimating correctly the noise fluctuations for our uncooled CCD camera. Note that

TABLE I
PARAMETER VALUES OF MODEL (18).

| $I_{D0}$ | $K_5$ | $K_6$ |
|---|---|---|
| 2.41 | $1.794\,10^{+5}$ | $2.31\,10^{-2}$ |

the long exposure time requires a frame integration time concept. Charges are collected simultaneously but are read out alternately. Changing the gate voltage shifts the image centroid by half a pixel in the vertical direction. This creates 50 % overlap, and therefore pixel sensitivity is doubled. This effect leads to an average of the noise.

E.2 Temperature calibration

In order to estimate the missing parameters of model (21), we have directly illuminated the camera by a nearly spatially uniform blackbody (see Figure 6). In order to cover a maximum of pixels, we have used a blackbody with a large cavity ($64\,mm$ aperture). The temperature range is from 20 to $550°C$. For a focal length $f$ of $8\,mm$, the F-number $N$ of 1.4, an integration time $ti$ of $360\,ms$ and an output amplifier gain $G_D$ of 1.41, we have computed the mean value ($I_D$) over a number of repeated image central regions (see Figure 7). Within these experimental conditions, a value of $I_D$ over the range $[0 - 255\,Gray\,Levels]$ involves a black-body temperature range from $300°C$ to $460°C$. Of course, with a lower time exposure value, it is possible to increase the blackbody temperature without signal saturation.

Using these experimental points $(T, I_D)$, the calibration procedure to estimate the $A_3$, $B$, $K_1$, $K_2$, $K_3$ and $K_4$ parameters of the model (21) is:

Fig. 6. Experiment for radiometric calibration.

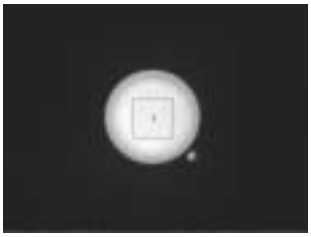

Fig. 7. (1) black-body uniform region.

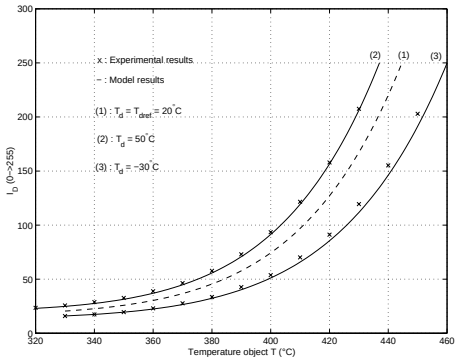


Fig. 8. Calibration and verification curves for different $T_d$.

1. *For the reference detector temperature $T_{dref}$: $A_3$ and $B$ determination.*
Usually, the manufacturer gives data at a reference temperature $T_{dref}$ of $20°C$. In this case, the correction function $f(\lambda_e, T_d)$ of the detector temperature is a unitary function in model (21). Curve 1 of Figure 8 shows experimental points and the model with $A_3$ and $B$ estimated parameters.
2. *For a different temperature $T_d$: $K_1$, $K_2$, $K_3$ and $K_4$ determination.*
With a temperature different from $T_{dref}$, knowing $A_3$ and $B$ parameters, we can estimate the parameters of the function $f(\lambda_e, T_d)$. The results of the experiment and estimation procedure obtained with a detector temperature $T_d$ of $50°C$ are plotted in curve 2 of Figure 8.
3. *Experimental verification of the model (21)*:
Considering the previous fitted parameters of model (21) and for a different value $T_d$ of $-30°C$, curve 3 of Figure 8 represents experimental and computed results. The difference between the experimental and calculated curve is lower than 1 % of the object temperature. Including all uncertainties, the model (21) with fitted parameters provided in Table II can be accepted.

TABLE II
PARAMETER VALUES OF MODEL (21).

| $A_3$ | $B$ | $K_1$ | $K_2$ | $K_3$ | $K_4$ |
|---|---|---|---|---|---|
| $1.011\,10^{+12}$ | $1.505\,10^{+4}$ | 1.743 | 1.396 | 0.631 | 1.018 |

*F. Performances*

Our experiments have taken into account detector temperature variations in the radiometric model (21) over a range from $-30°C$ to $50°C$. We model effects related to detector temperature in quantum efficiency due to variation in light absorption. In the reference of absorption coefficient formulas [13], the model can be extended to detector temperatures lower than $-30°C$ down to $-50°C$. At the other end, for temperatures higher than $50°C$ up to $80°C$ (CCD detector is still operating), no experiment shows the validity of the model.

However, we can observe a high level of dark current (see Figure 5).
Knowing the detector temperature with an external sensor, the radiometric model (21) allows object temperature correction of $25°C$ for a gray level value of 100 (see Figure 8).
Particularly, in a measurement context, it is important to qualify the radiometric model performances in terms of signal-to-noise ratio ($SNR$) and Noise Equivalent Temperature Difference ($NETD$) as functions of detector temperature $T_d$. Our goal, described in the introduction, is to measure a low object temperature $T$ of $350°C$ with uncertainty value of $\pm 25°C$. At this object temperature, Figure 9 illustrates the signal-to-noise ratio ($SNR$) as a function of the temperature detector $T_d$ for different exposure times. The signal is provided

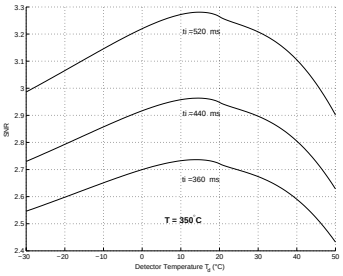


Fig. 9. $SNR$ as function of $T_d$.

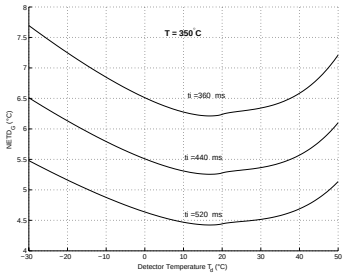


Fig. 10. $NETD$ as function of $T_d$.

by model (21), and the square root of the noise variance comes from the model (20). We observe a maximum of $SNR$ at a detector temperature $T_d$ of $18°C$. Below this temperature value, the quantum efficiency limits the $SNR$ value. At high detector temperature, dark current dominates and the $SNR$ decreases. The $NETD$ criterion is defined as the ratio of the standard deviation noise to the sensitivity that represents the derivative radiometric model (21) in function of object temperature $T$. We compute it for an object temperature $T_0$ of $350°C$. The result of $NETD$ versus temperature and for different exposure time is plotted in Figure 10. In the same way, $NETD$ curves present also a minimum at the detector temperature of $18°C$. For a low detector temperature, sensitivity increases more than noise. On the contrary, for a high detector temperature, noise dominates.
As a conclusion, high detector temperatures degrade camera performances, but it is possible to adjust exposure time $ti$ to respect values of $SNR$ or $NETD$. For example, at the reference detector temperature, to measure over the range from $350°C$ to $1000°C$ with signal-to-noise ratio $SNR$ higher than 2 and the $NETD$ value always higher than $8°C$, five exposure times are required over the range from $0.36\,s$ to $1/10000\,s$. The value of F-number $N$ and amplifier output gain $G_D$ are the same as those used in experiments.

## III. Geometric model

This section describes the geometric model of the imaging system (optical lens, camera and digital card). After an overview of the "pin-hole" model used in our applications, we define their extrinsic and intrinsic parameters to be calibrated. Extrinsic parameters describe the transformation of the object $3D$ frame into the camera $3D$ frame. The transformation of the latter frame into the image $2D$ frame is expressed by intrinsic parameters. They depend on optic perspective projection and detector CCD spatial resolution. By studying the Modulation Transfer Function $MTF$, we examine the influence of spectral band and detector temperature on the spatial resolution. This analysis shows that intrinsic parameters depend on spectral band and detector temperature. In this section, we do not discuss the accuracy of intrinsic parameters in function of $3D$ error models or $2D$ errors introduced by the target detection in the camera image [14].

### A. "Pin-hole" model

The basic assumption of the "pin-hole" model is that the lens center $O_{cam}$ is the intersection of all optical beams. We assume that the image plane (or $CCD$ detector plane) is perpendicular to the optical axis $(O_{cam} - z)$. Figure 11 illustrates the basic geometry of the pin-hole camera model. $R_{obj}(0_{obj}, \vec{X}, \vec{Y}, \vec{Z})$ represents the object $3D$ frame, while $R_{cam}(0_{cam}, \vec{x}, \vec{y}, \vec{z})$ denotes the camera $3D$ frame, and $R_{im}(0_{im}, \vec{u}, \vec{v})$ is

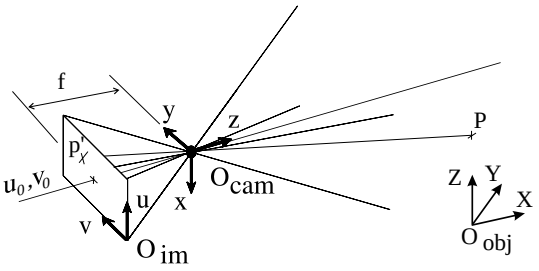


Fig. 11. Object and camera coordinate system.

the image $2D$ frame. Finally, $(u_0, v_0)$ is the principal point, or the optical center ($0_{cam}$) projection on the $CCD$ detector plane.

Three steps are required to compute the transformation from a point $P(X,Y,Z)$ in $R_{obj}$ to a point $p^{'}(u,v)$ in $R_{im}$:

1. Rigid body transformation (rotation $R$ and translation $T$) of the object coordinates $(X,Y,Z)$ in $R_{obj}$ to camera coordinates $(x,y,z)$ in $R_{cam}$.

2. Perspective projection with center $0_{cam}$, axis $\vec{z}$ and ratio $f$ (distance between the CCD detector and the optical center), of the $3D$ point $(x,y,z)$ into an image point $(i,j,f)$ expressed in the camera $3D$ frame.

3. Transformation of camera coordinates $(i,j,f)$ into $2D$ image frame coordinates $(u,v)$ using an origin transformation $(u_0, v_0)$ in the image plane and a space sampling according to the pixel sizes $\Delta x$ and $\Delta y$ (considering pixels as adjacent in the CCD array). The dependence of pixel sizes on wavelength and detector temperature will be discussed in paragraph III-B.

By combining these three steps, model (22) relates the transformation of the $3D$ object into the $2D$ image frame.

$$\begin{pmatrix} u \\ v \end{pmatrix} = \begin{pmatrix} u_0 \\ v_0 \end{pmatrix} + \begin{pmatrix} \frac{f}{\Delta x(\lambda,T_d)} \frac{R_{11}X+R_{12}Y+R_{13}Z+T_x}{R_{31}X+R_{32}Y+R_{33}Z+T_z} \\ \frac{f}{\Delta y(\lambda,T_d)} \frac{R_{21}X+R_{22}Y+R_{23}Z+T_y}{R_{31}X+R_{32}Y+R_{33}Z+T_z} \end{pmatrix} \tag{22}$$

Model (22) involves 12 extrinsic parameters (9 for rotation $R$ and 3 for translation $T$) and 4 intrinsic parameters ($u_0, v_0$, $\alpha_u = \frac{f}{\Delta x(\lambda,T_d)}$, $\alpha_v = \frac{f}{\Delta y(\lambda,T_d)}$). To simplify the presentation, we do not introduce in this paper the lens distortion correction step described in [15]. We use this correction in our applications.

The model calibration described in [8] or [16] involves a computation of the camera extrinsic and intrinsic parameters based on several points whose object coordinates $(X,Y,Z)$ in the $3D$ object frame $R_{obj}$ are known and whose image coordinates $(u,v)$ are measured. These points are extracted from several images of a specific object (planar calibration pattern), moved in front of the camera.

For robotic applications, self-calibration methods [17] have been proposed to recover these parameters on line, using a weak camera model. For our measurement applications, we apply a strong calibration method, which requires two steps: (a) using initial estimates of the intrinsic parameters computed from the camera characteristics, the object pose computation [18] gives estimates for the extrinsic parameters for each image acquired on the calibration object. (b) Then, from the initial guesses, a nonlinear minimization method (including the estimation of the distortion coefficients) allows improving the estimation of these parameters. A basic hypothesis for this procedure is that focal length $f$ and pixel sizes $\Delta x$ and $\Delta y$ remain constant. If it is not the case (active camera or fluctuations according to the wavelength and to the detector temperature), they must be estimated again.

The metrology applications require very accurate estimates of the camera parameters: therefore we have to verify if intrinsic parameters, especially $\alpha_u = \frac{f}{\Delta x}$ and $\alpha_v = \frac{f}{\Delta y}$, are changing with spectral band and detector temperature fluctuations. The Modulation Transfer Function ($MTF$) of the camera characterizes the optic effects and how the discrete locations of detector elements $(\Delta x, \Delta y)$ sample spatially the scene in function of wavelength and detector temperature.

### *B. Camera Modulation Transfer Function MTF*

The complete $MTF$ of the camera is the product of the optic $MTF$ ($MTF_o$) and the detector $MTF$ ($MTF_d$), that is:

$$MTF = MTF_o \times MTF_d \tag{23}$$

#### B.1 Optic Modulation Transfer Function $MTF_o$

With reference to [19], $MTF_o$ in the horizontal or vertical direction of a radial symmetric optical system with a clear circular diffraction-limited aperture illuminated monochromatically is given by:

$$MTF_o(f_s) = \frac{2}{\pi}\left(\cos^{-1}\left(\frac{f_s}{f_{oc}}\right) - \left(\frac{f_s}{f_{oc}}\right)\sqrt{\left(1-\left(\frac{f_s}{f_{oc}}\right)^2\right)}\right) \tag{24}$$

where $f_{oc}$ is the cutoff frequency of the optical system ($f_{oc} = \frac{1}{N\lambda}$). In $NIR$ spectral band, with an F-number $N$ equal to 1.4, $MTF_o$ is close to 1 ($0.998 - 0.978$). The camera $MTF$ can then be approximated by $MTF_d$.

$$MTF \approx MTF_d \tag{25}$$

The camera cutoff frequency $f_c$ is equal to the detector cutoff frequency $f_{dc}$.

#### B.2 Detector Modulation Transfer Function $MTF_d$

The CCD detector is a spatial sampler of a horizontal frequency $f_{Hs}$ (respectively vertical $f_{Vs}$) of the input signal. The highest CCD horizontal frequency reproduced is the Nyquist horizontal frequency $f_{HN}$ (respectively vertical $f_{VN}$). It is mandatory that the input signal frequency be inferior to the Nyquist frequency to respect the Shannon theorem and to avoid spatial aliasing. In metrology applications, the Nyquist frequency is the band-limit or the system cutoff frequency $f_{dc}$ which is defined as half an inverse pixel dimension: $f_{HN} = \frac{1}{2\,\Delta x}$ (respectively $f_{VN} = \frac{1}{2\,\Delta y}$). We assume here that pixels are adjacent. We note that the detector cutoff frequency decreases when the cell area increases.
Moreover of the influence of the detector geometry, in $NIR$ spectral band, the photon absorption occurs at increasing depths along the substrate detector depth $z$. The absorption law $\Phi$ approaches an exponential law ($\Phi = C^t \exp(-\alpha\, z)$) where the coefficient absorption $\alpha$ in the silicon decreases with an increasing wavelength (see Figure 3). However, the depletion region size $ZD$ is finite (see Figure 2), and the majority of long wavelength photons will be absorbed outside of the depletion region. An electron generated in the substrate will experience a three-dimensional random walk until it recombines or reaches the edge of the neighbor depletion region. In the last case, this phenomenon, called diffusion, creates a response that overlaps other pixels (see Figure 12 in reference of [13]).
Finally, in $NIR$ spectral band, the detector $MTF$ ($MTF_d$) results from the product of the geometric $MTF$ ($MTF_{geo}$) by the diffusion $MTF$ ($MTF_{diff}$) and it is expressed by:

$$MTF_d = MTF_{geo} \times MTF_{diff} \tag{26}$$

According to [20], the geometric $MTF_{geo}$ of a single CCD cell is given by:

$$MTF_{geo}(f_{Hs}, f_{Vs}) = \left|sinc(\pi\,\frac{f_{Hs}}{2\,f_{HN}})\right|\left|sinc(\pi\,\frac{f_{Vs}}{2\,f_{VN}})\right| \tag{27}$$

In order to simplify the expression, we compute the $MTF_{geo}$ only in one dimension for the horizontal direction $x$. Therefore we denote the horizontal input frequency $f_{sH}$ as $f_s$ and horizontal Nyquist frequency $f_{HN}$ as $f_N$. For $f_N = f_{dc} = f_s$, the $MTF_{geo}$ value is 0.637.
For a front illuminated CCD, the diffusion term $MTF_{diff}$ in reference of [21] can be written as:

$$MTF_{diff}(\lambda, T_d) = \frac{1 - \frac{\exp\left(-\alpha(\lambda,T_d)\,\chi_p\right)}{1+\alpha(\lambda,T_d)\,Lo(f_s)}}{1 - \frac{\exp\left(-\alpha(\lambda,T_d)\,\chi_p\right)}{1+\alpha(\lambda,T_d)\,L_n}} \tag{28}$$

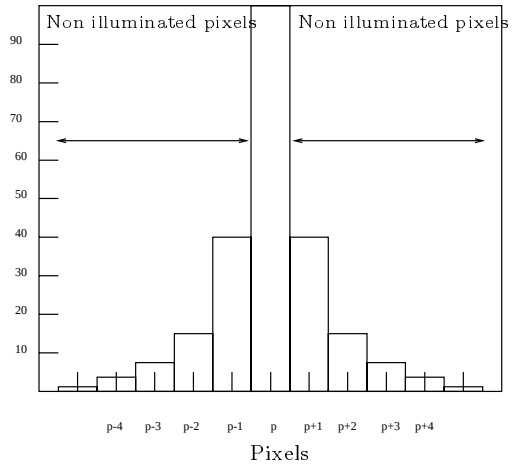


Fig. 12. Diffusion influence.

where the factor $Lo$ is the spatial frequency-dependent component of diffusion length $L_n$ ($Lo = \frac{L_n}{\sqrt{1+(2\pi L_n f_s)^2}}$) and $\chi_p$ is the depletion width (see Figure 2).
Let us remark that the diffusion term $MTF_{diff}$ depends on the absorption coefficient as a function of wavelength and temperature as shown in Figure 3.
Figure 13 shows $MTF_{diff}$ versus wavelength ($\chi_p = 4\,\mu m, L_n = 7.1\,\mu m$). For short wavelengths ($\lambda < 0.6\mu m$),

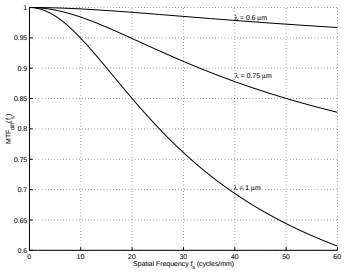


Fig. 13. $MTF_{diff}$ as a function of $\lambda$.

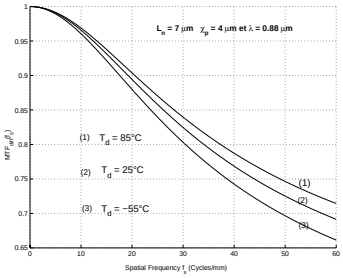


Fig. 14. $MTF_{diff}$ as a function of $T_d$.

$MTF_{diff}$ can be neglected and it approaches 1 ($MTF_d \approx MTF_{geo}$). For the $NIR$ spectral band ($\lambda > 0.75\mu m$), the diffusion term $MTF_{diff}$ dominates in the $MTF_d$ relation. As illustrated by Figure 14, the diffusion term $MTF_{diff}$ decreases with the detector temperature.
As a conclusion, in the visible spectral band, we can approximate the camera $MTF$ with only the geometric $MTF$ ($MTF_{geo}$) of the detector:

$$MTF = MTF_d = MTF_{geo} \tag{29}$$

But, in $NIR$ spectral band, the camera $MTF$ must be expressed as the product of the geometric $MTF$ ($MTF_{geo}$) by the diffusion $MTF$ ($MTF_{diff}$).

$$MTF = MTF_d = MTF_{geo} \times MTF_{diff} \tag{30}$$

With the same value of $MTF$ ($MTF = 0.637$), the camera cutoff frequency $f_c$ is lower in $NIR$ than in visible spectral band. In addition, its value decreases with the detector temperature. Finally, the pixel effective sizes ($\Delta x = \frac{1}{2\,f_c}$) are higher in $NIR$ than in visible spectral band.

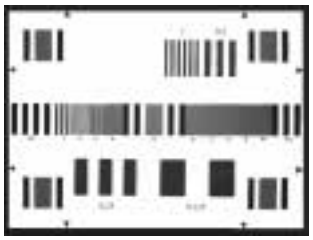

Fig. 15. Bar test target.

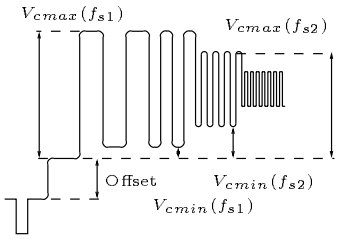


Fig. 16. Definition of $V_{cmax}$ and $V_{cmin}$.

### C. Experimental results

Although the camera $MTF$ is defined for sinusoidal signals, the square wave (see Figure 15) is the most popular test target. The system response to a square-wave target is the Contrast Transfer Function ($CTF$).

$$CTF(f_s) = \frac{V_{cmax} - V_{cmin}}{V_{cmax} + V_{cmin}} \tag{31}$$

where $V_{cmax}$ and $V_{cmin}$ are respectively maximum and minimum signal levels of the white and black bar test (see Figure 16). To obtain the relationship between square wave and sinusoidal amplitude, we have to express the square wave as a cosine series. The output amplitude is an infinite sum of input cosine amplitudes modified by $MTF$.

$$CTF(f_{s0}) = \frac{4}{\pi}\left|MTF(f_{s0}) - \frac{MTF(3\,f_{s0})}{3} + \cdots\right| \tag{32}$$

where $f_{s0}$ represents the fundamental frequency of the square wave.
For a bar target with spatial frequency $f_s$ above 1/3 of the frequency computed to $MTF = 0$, we can write the camera $MTF$ from the measured $CTF$ as follows:

$$MTF = \frac{\pi}{4}\,CTF \tag{33}$$

After measuring the $CTF$ of the $VHR2000$ CCD camera tested in paragraph II-E, from relation (33) we compute the $MTF$, and we compare the cutoff frequency $f_c$ (for a value of 0.637 of the $MTF$) in visible and in $NIR$ spectral band. We also examine the influence of the detector temperature on the $MTF$.

C.1 $MTF$ as a function of wavelength:

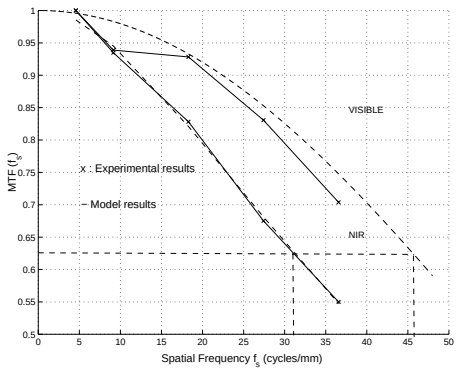


Fig. 17. Experimental verification of $MTF$.

Using experimental and model results ($MTF, f_s$) plotted in Figure 17, we can compute the cutoff frequency $f_c$:

- *in visible spectral band* ($MTF_{diff} \approx 1$):

For a value of 0.637 of the $MTF$, the value of the cutoff frequency $f_c$ is $45.3 cycles/mm$. From relation ($\Delta x = \frac{1}{2\,f_c}$), it easily follows that the value of the detector width $\Delta x$ is $11\mu m$ . The value is different from the manufacturer's ($\Delta x = 8.6\mu m$) due to a low-pass filter with a cutoff frequency lower than the Nyquist frequency to satisfy the Shannon sampling theorem.

- *in $NIR$ spectral band*:

Considering experimental results plotted in Figure 17, $MTF$ produced in $NIR$ is lower than $MTF$ produced in visible spectral band. We can estimate $L_n$ and $\chi_p$ parameters of the diffusion term $MTF_{diff}$ (28) in the model (30). The values are provided in Table III. As a result, the value of the cutoff frequency $f_c$ is $30.50\,cycles/mm$, and leads to a detector width value $\Delta x$ of $16.39\mu m$.

TABLE III
PARAMETER VALUES OF MODEL (28).

| $L_n\,(\mu m)$ | $\chi_p\,(\mu m)$ |
|---|---|
| 7.101 | 3.36 |

We note that the diffusion length value $L_n$ is small. The limited diffusion in the substrate stems from an epitaxial layer in $ICX039$ detector.

As a conclusion, in $NIR$ spectral, $MTF$ decreases and it is equivalent to work with detector sizes 1.34 times higher.

C.2 $MTF$ as a function of the detector temperature:

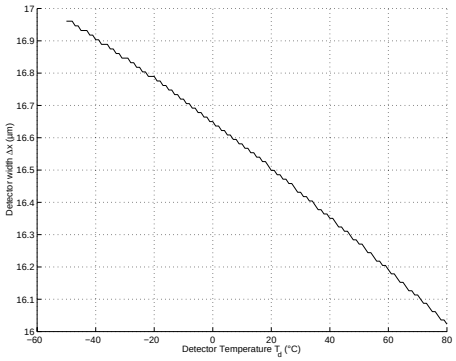


Fig. 18. $\Delta_x$ as a function of $T_d$.

To take into account the effects of the detector temperature, considering previous values of $L_n$ and $\chi_p$ parameters (see Table III), we compute the absorption coefficient $\alpha$ (see formulae in Appendix) as a function of detector temperature $T_d$ ranging from $-50°C$ to $80°C$. From these computations and the model (30) in $NIR$ spectral band, we obtain the $MTF$ values versus temperature $T_d$. For $MTF$ value of 0.637, we can deduce the cutoff frequency $f_c$ and compute the detector width ($\Delta x = \frac{1}{2\,f_c}$) as a function of $T_d$. The Figure 18 shows a linear decreasing of the detector width $\Delta x$ with a detector temperature increasing $T_d$. We can infer the following linear model:

$$\Delta_x(T_d) = \Delta_x(T_{dref}) - K_7\,(T_d - T_{dref}) \tag{34}$$

where $K_7$ is a parameter whose value ($K_7 = 7.235\,10^{-3}$) has been obtained from the experimental points plotted in Figure 18.

### D. Performances

By studying the $MTF$ as a function of wavelength, we notice that the spatial resolution of the CCD detector decreases with an increasing of wavelength to account for diffusion phenomenon. To fit the intrinsic parameters of the "pin-hole" camera model, the system has been calibrated in $NIR$ spectral band.
The same studies show an increasing of spatial resolution with detector temperature. We propose a correction law (34) of intrinsic parameters $\alpha_u$ and $\alpha_v$ as a function of detector temperature $T_d$. With a limited substrate detector by an epitaxial layer, the correction is less necessary than with a thick substrate detector (for example, with the detector Hamamatsu $S5466$). The model calibration has been tested in visible and in $NIR$ spectral band with test points extracted from lozenge center. We estimate intrinsic parameters with method [16], and we obtain $\alpha_u$ and $\alpha_v$ 1131.17 and 1037.34 in visible, and respectively 1139.53 and 1045.09 in $NIR$ spectral band. The localization error given by the method described in [18] is $0.1\,mm$ at an observation distance of $1\,m$. This experiment should be conducted many times to verify parameter dispersion.

## IV. Two models interests

In the two previous sections, we have presented radiometric and geometric calibration procedures for an uncooled CCD camera. We emphasize the fluctuations of the camera parameters with respect to the detector temperature and to the wavelength.
In this section, we show the interest of these two models in order to improve some measurements on a hot object, which can be in any situation in the view field of the camera. In fact, variable orientation $\theta_s$ and distance $d_s$ of a hot object could be estimated by a $3D$ localization. For monocular vision (only one camera),

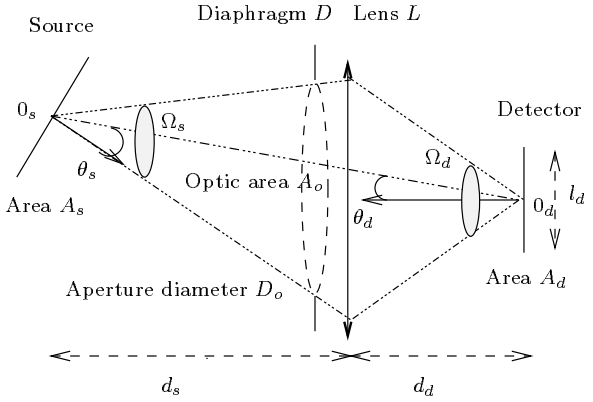


Fig. 19. Description of geometric situation.

it could be impossible to locate a single hot point. This point must be associated to a surface belonging to an object. The object position with respect to the camera can be computed only if the $3D$ geometric model of the object has been previously learned. For an application concerning the monitoring of free-form objects, a rigid visual pattern can be fixed on the object to make this localization easier by using a classical method [8].
For multi-ocular vision (passive stereo vision), a hot point could be detected and localized using triangulation methods. But, it is required that this point is in the view field of the two cameras. A first estimate on the radiometric attributes, computed without any knowledge on the orientation and the distance, could be used as a stereo-matching criterion. Then, once the point distance is known, the orientation could be computed from local planar approximations, and the radiometric attributes could be refined using the equation 36.
In fact, the Figure 19 shows the geometric situation between a hot source (black body) of area $A_s$ and sensor of area $A_d$ through the optical system of focal length $f$ and area $A_o$. The hot source sees optical area $A_o$ under the solid angle $\Omega_s = \frac{A_o}{d_s^2}$ (in the same way the detector sees optical area $A_o$ under the solid angle $\Omega_d = \frac{A_o}{d_d^2}$). $\theta_s$ is the angle between the axis $0_s - 0_d$ and the source normal $\overrightarrow{N_s}$ (respectively $\theta_d$ with detector normal $\overrightarrow{N_d}$).
In a measurement situation, angles $(\theta_s, \theta_d)$ are different from zero, the optical system is not focused, and we

have to correct the digital output signal measurement $I_{Dmes}$ by the geometric situation as follows:

$$I_D = \frac{I_{Dmes}}{\frac{A_s f^2 cos(\theta_s)}{A_d d_s^2}} \tag{35}$$

where $\theta_s$, $d_s$ and $A_s$ are provided by localization methods. After correction of $I_{Dmes}$ in relation (35), the radiometric model is inverted to measure the object temperature $T$ with respect to the corrected intensity $I_D$. The relation (36) provides the real object temperature $T$.

$$T = \frac{B}{\ln\left(\frac{A_3 \frac{G_D{}^{ti}}{N^2} f(T_d)}{I_D - D(T_d)} + 1\right)} \tag{36}$$

With any hot source, we must also modify $I_{Dmes}$ by emissivity value $\varepsilon$ at effective wavelength $\lambda_e$. It is better to work with a short wavelength to decrease uncertainty on this emissivity. For example, in [22], a relative emissivity uncertainty $\frac{\Delta\varepsilon}{\varepsilon}$ of 20% leads to a relative temperature uncertainty $\frac{\Delta T}{T}$ of 1.2% at wavelength $\lambda_e = 1\mu m$ and of 12% at $\lambda_e = 10\mu m$ respectively.

## V. Conclusion

In this paper, we have described radiometric and geometric models taking into account detector temperature variations based on an uncooled low-cost CCD camera operating in the Near Infrared spectral band ($NIR$).

Using physical CCD properties, we have analyzed the influence of wavelength and detector temperature fluctuations on the radiometric model (see formula (21)) usually used in cooled infrared thermographic systems. The temperature fluctuations (a) involve quantum efficiency variations due to light absorption and modifications of diffusion mechanisms (see equation (13)); and (b) affect sensor noise levels (see relation (18)) (especially dark current). Experimental calibration results confirm the radiometric model (21) with a CCD camera based on a Sony detector over a detector temperature range of $-30°C$ to $50°C$. Knowing the detector temperature with an external sensor, this model allows us to correct the object temperature by 10% (see Figure 8) to compensate detector temperature fluctuations of $80°C$. To obtain the same performances in function of detector temperature variation in terms of Signal Noise Ratio ($SNR$) or Noise Equivalent Temperature Difference ($NETD$), we propose to adjust the exposure time of the CCD detector. Figures 9 and 10 show $SNR$ and $NETD$ respectively as a function of detector temperature $T_d$. An optimal point of both criteria at a detector temperature of $18°C$ can be exhibited. Moreover, we can measure a hot object over the temperature range of $350°C$ to $1000°C$ with a precision lower than $\pm 25°C$ at $350°C$.

On the other hand, by studying the Modulation Transfer Function ($MTF$), we have analyzed the detector CCD spatial resolution properties in function of spectral band and detector temperature fluctuations. This analysis establishes that the spatial resolution decreases in $NIR$ spectral band due to a diffusion term $MTF_{diff}$ (see formula (28)). This term ($MTF_{diff}$) depends on the absorption coefficient that is itself wavelength and detector temperature dependent. Therefore, we prove that the spatial cutoff frequency $f_c$ of a CCD detector decreases when the wavelength increases and the detector temperature decreases. As the cutoff frequency is inversely proportional to pixel size $\Delta x$ ($f_c = \frac{1}{2\,\Delta x}$), it is equivalent to work with an effective pixel size which is wavelength and detector temperature dependent. The properties are explained in geometric model (22). First of all, to consider wavelength effects, we have to calibrate the model in $NIR$ spectral band to fit intrinsic parameters with effective pixel sizes. Then, using model (34), the detector temperature correction can be applied in the geometric model (22) to compensate a relative error of 0.01% in a displacement of $100\,mm$. This error could be higher with a thick substrate detector with greater diffusion effects.

We have characterized a low-cost sensor to measure surface temperature field and dimensional characteristics. It could be used in the thermal treatment process of tools [23] or super plastic forming (SPF) of Titanium alloy sheets [24].

## Appendix

According to [13], the absorption photons coefficient is given by :
(a) For a photon energy $E$ between 1.2 and 2.2 $eV$ :

$$\alpha = 2750\Big(\frac{E - 1.1 + 5\,10^{-7}\,T_d^2}{\exp(348/T_d) - 1} + \frac{(E - 1.16 + 5\,10^{-7}\,T_d^2)^2}{1 - \exp(-348/T_d)}\Big) \tag{37}$$

(b) For a photon energy $E$ between 2.2 and 2.5 $eV$ :

$$\alpha = \alpha(2.2\,eV; T_d)\Big(\frac{7447.3}{\alpha(2.2\,eV; T_d)} + 0.4491\Big)^{(E/0.3 - 7.3333)} \tag{38}$$

## Acknowledgments

Many thanks are due to J.J. Orteu for his hepful comments. The authors wish to thank the Referees.

## References

[1] Y. Le Maoult, S. Baleix, P. Lours, and G. Bernhart, "Application industrielle de la thermographie infrarouge au comportement des outillages de formage superplastique," in *Congrès National sur les applications de la thermographie dans les industries mécaniques*, CETIM Senlis, France, 1999.

[2] D. Garcia and Jean Jose Orteu, "3D Deformation Measurement using Stereo-correlation applied to the Forming of Metal or Elastomer Sheets," in *International Workshop on Video-Controlled Materials Testing and In-Situ Microstructural Characterization*, Nancy (France), November 1999, Ecole des Mines de Nancy.

[3] S. Claudinon, P. Lamesle, Jean Jose Orteu, and R. Fortunier, "Continuous in-situ measurement of quenching distortions using computer vision," *submitted to Journal of Materials Processing Technology*, 2000.

[4] G.J. Zissis, Ed., *Sources of Radiation*, vol. 1 of *The infrared & Electro-Optical Systems Handbook*, SPIE Press, Environmental Researh Institute of Michigan, 1992.

[5] F. Moreau, *Thermographie proche infrarouge par caméras CCD et application aux composants de première paroi du Tokamak TORE SUPRA*, Thèse de doctorat, Université de Saint Jérôme - Aix-Marseille III, June 1996, Euratom-CEA.

[6] F. Mériaudeau, E. Renier, and F. Truchetet, "Uncertainty committed on temperature measurement," in *Congrès International de Métrologie*, Nimes, France, October 1995, vol. 1, pp. 189–194.

[7] Glenn E. Healey and R. Kondepudy, "Radiometric CCD Camera Calibration and Noise Estimation," *IEEE Transactions on Pattern Analysis and Machine Intelligence*, vol. 16, no. 3, pp. 267, March 1994.

[8] R.Y. Tsai, "A Versatile Camera Calibration Technique for Hight-Accuracy 3D Machine Vision Metrology Using Off-the-Shelf TV Cameras and Lenses," *IEEE Journal of Robotics and Automation*, vol. RA-3, no. 4, August 1987.

[9] P. Saunders and T. Ricolfi, "The characterisation of a CCD camera for the purpose of temperature measurement," in *TEMPMEKO'96 - International symposium on temperature and thermal measurement in industry and science*, Torino, Italy, September 1996, pp. 329–334.

[10] M. Orgeret, *Les piles solaires, le composant et ses applications*, Editions Masson, 1985.

[11] F.H. Gaensslen, V.L. Rideout, E.J. Walker, and J.J. Walker, "Very Small MOSFET's for Low Temperature Operation," *IEEE Transactions Electron Devices*, vol. ED-24, pp. 218–229, March 1977.

[12] S. P. Emmons, R. W. Brodersen, J. B. Barton, C. R. Hewes, and D. D. Buss, "A Study of Noise in Charge-Coupled Devices," Tech. Rep., Texas Instruments Incorpored, Central Research Laboratories 13 500 N. Central Expwy., Dallas, Texas 75222, May 1975.

[13] G. Rolland, "Etude des variations de rendement quantique interne d'un détecteur CCD en fonction de la température," *Revue de Physique Appliquée*, , no. 20, pp. 651–659, September 1985.

[14] J.M. Lavest, M. Viala, and M. Dhome, "Do you really need an accurate calibration pattern to achieve a reliable camera calibration ?," in *European Conference on Computer Vision (ECCV'98)*, Freiburg (Gernany), June 1998, vol. 1, pp. 158–174.

[15] G. Weng, S. Ma, and M. Herniou, "Camera Calibration with Distorsion Models and Accuracy Evaluation," *IEEE transactions on Pattern Analysis and Machine Intelligence*, vol. 14(10), pp. 965–980, October 1992.

[16] M. Devy, V. Garric, and J. J. Orteu, "Camera calibration from multiple views of a 2D object, using a global non linear minimization method," in *IEEE/RSJ International Conference on Intelligent Robots and Systems (IROS'97)*, Grenoble (France), 8-12 Septembre 1997.

[17] A. Fusiello, "Uncalibrated Euclidean reconstruction : a review," *Image and Vision Computing*, vol. 18, pp. 555–563, May 2000.

[18] M.A. Abidi and T. Chandra, "A New Efficient and Direct Solution for Pose Estimation Using Quadrangular Targets : Algorithm and Evaluation," *IEEE Transactions on Pattern Analysis and Machine Intelligence*, vol. 17, no. 5, pp. 534–, May 1995.

[19] M. C. Dudzik, Ed., *Electro-Optical Systems Design, Analysis, and Testing*, vol. 4 of *The infrared & Electro-Optical Systems Handbook*, SPIE Press, Environmental Research Institute of Michigan, 1992.

[20] G. C. Holst, *CCD Arrays Cameras and Displays*, SPIE Optical Engineering Press, Bellingham, Washington USA, 1998.

[21] D. H. Sieb, "Carrier Diffusion Degradation of Modulation Transfer Function in Charge Coupled Imagers," *IEEE Transactions on Electron Devices*, vol. ED-21(5), pp. 210–217, 1974.
[22] J. Martinet, *La mesure des températures par rayonnement thermique*, Bureau National de Métrologie, 1981.
[23] S. Claudinon, *Contribution à l'étude de la distorsion des aciers au traitement thermique : Suivi en continu par vision artificielle et simulation numérique*, Ph.D. thesis, Ecole des Mines Paris, Février 1999.
[24] S. Baleix, *Oxydation et écaillage d'alliages réfractaires moules pour outils de formage superplastique*, Ph.D. thesis, Université Paul Sabatier-Toulouse III, Décembre 1999.

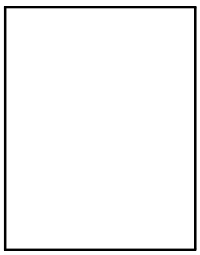

**Thierry Sentenac** received a M.S degree in computer science from INP Toulouse in 1992. From 1992 to 1995, he was a research engineer at LAAS-CNRS in Toulouse (France) where he is currently a PhD Student. Since 1995, he has been also working as an Associate Professor and he is head of the Electrical Engineering department at the Ecole des Mines d'Albi (Albi, France) specialized in process engineering.
His current research interest cover CCD image processing, computer vision and optoelectronic

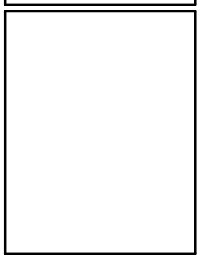

**Yannick Le Maoult** received a M.S degree in physical measurements from INP Grenoble in 1987. Working as an engineer in a research company and in the L.R.C-CNRS (Marseille, France) on advanced infrared radiometry applied to combustion, he received his PhD degree from University de Provence (Marseille, France) in 1992. Since 1992, Dr Le Maoult has been working as an associate professor at the Ecole des Mines d'Albi, a french Grande Ecole specialized in Process engineering. Member of the Computer Vision and IR thermography group (Material Research Center), his fields of interest are especially : Radiative Transfer, Optical Measurements, Metrology and Inverse Methods; he is particularly involved in infrared measurements such as thermography or pyrometry applied to material processing or reactive flows.

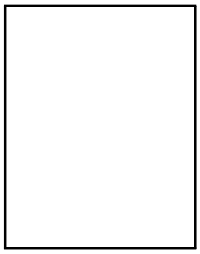

**Guy Rolland** has been working as an engineer at CNES (French national centre for space research) since 1978. From 1978 to 1987 he worked in the field of characterisation and physical modelling of CCD, and other detectors, for earth observation and scientific satellites. From 1987 to 1999 he concentrated his activities in the field of modelling CCD and active electronics components by the means of finite elements methods (process and devices simulations). Since 1999, he has been working in the field of radiation effects on components and systems. One of his today research themes is the effect of space radiation on CCD. He also teaches the physics of semiconductors imaging components in Toulouse university and engineer schools.

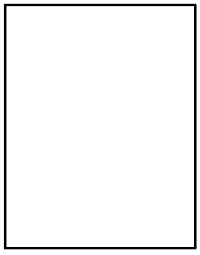

**Michel Devy** got his degree in Computer Science Engineering in 1976 from IMAG, in Grenoble (France). He received is Ph.D. in 1980 from LAAS-CNRS in Toulouse (France). Since 1980, he has participated to the Robotics and Artificial Intelligence group of LAAS-CNRS; his research is devoted to the application of computer vision in Automation and Robotics. He has been involved in numerous national and international projects, about Manufacturing Applications, Mobile Robots for space exploration or for civil safety, 3D Vision for Intelligent Vehicles or Medical applications, .... He is now Research Director at CNRS, head for the Perception Area in the Robotics Group of LAAS-CNRS and his main scientific topics concerns Perception for Mobile Robots in natural or indoor environments.